Experimental hysteretic behavior of in-plane loaded reinforced grouted multi-ribbed aerated concrete blocks masonry walls

Sheng-Cai Li*, Jian-Xi Dong and Li-Feng Li

School of Civil Engineering, Huaqiao University, Quanzhou, China

Abstract. In order to analyze the experimental hysteretic behavior of the in-plane loaded reinforced grouted multi-ribbed aerated concrete blocks masonry walls (RGMACBMW), we have carried out the pseudo static testing on the six specimens of RGMACBMW. Based on the test results and shear failure characteristics, the shear force hysteretic curves and displacement envelope curves of the models were obtained and discussed. On the basis of the hysteretic curves a general skeleton curve of the shear force and displacement was formed. The restoring model was adopted to analyze the seismic behavior and earthquake response of RGMACBMW. The deformation capacity of the specimens was discussed, and the formulas for calculating the lateral stiffness of the walls at different loading stages were proposed as well. The average lateral displacement ductility factor of RGMACBMW calculated based on the test results was 3.16. This value illustrates that if the walls are appropriately designed, it can fully meet the seismic requirement of the structures. The quadri-linear restoring models of the walls degradation by the test results accurately reflect the hysteretic behaviors and skeleton curves of the masonry walls. The restoring model can be applied to the RGMACBMW structure in earthquake response analysis.

Keywords: RGMACBMW, pseudo static test, deformation behavior, stiffness, restoring model

1. Introduction

RGMACBMW is a new structural bearing member with perfect properties such as light weight, high strength, low energy consumption and good seismic capacity (Li and Zeng 2005). This type of wall is composed of insulation energy-saving blocks and an invisible multi-ribbed frame, whose load-bearing capacity and seismic performance are different from common concrete members. There has been much researched done on reinforced concrete masonry walls. The flexural and shear strength behaviors of reinforced concrete masonry walls subject to both monotonic and cyclic lateral loads are examined based on experimental results obtained from 22 specimens of 6ft x 6ft masonry wall sections (Shing *et al*. 1990a, b). Thirty-six panels were examined to investigate the in-plane behavior of grouted concrete masonry walls under well-defined bi-axial tension-compression loading conditions (Drysdale and Khattab 1995). To provide data for the masonry wall panels, a bi-axial test frame was constructed capable of loading

---

*Corresponding author, Professor, E-mail: lsc50605@hqu.edu.cn

masonry panels 80 cm high by 120 cm wide in tension and compression combination (Tikalsky *et al.* 1995). The tensile behavior of reinforced concrete and clay unit masonry members were studied by conducting a series of 33 direct tension tests on instrumented specimens (Atkinson and Hammons 1997). Ten single-story concrete masonry wall panels were tested at the University of Auckland in order to examine the in-plane shear strength of concrete masonry walls constructed using New Zealand masonry units utilizing pumice aggregate and assembled using common local construction techniques and establish its design expression (Voon and Ingham 2006, 2007). Through reversed cyclic lateral loading tests on six full-scale walls, the failure processes were analyzed. The effects of the amount and distribution of vertical reinforcement and the level of axial compressive stress on the inelastic behavior and ductility were investigated (Shedid *et al.* 2008, 2009). The different factors influencing the reliability of reinforced grouted concrete block masonry in compression are studied, including model error, grouted block masonry strength, load effect combinations, eccentricity, reinforcement ratio, live load type, structural safety class, live-to-dead load ratio and discretization of wall thickness, and a probabilistic model to calculate the structural reliability of typical reinforced grouted concrete block masonry walls designed to Chinese standards, loaded concentrically and eccentrically in compression is developed (Zhai and Stewart 2010). In order to study the ductility and the lateral load carrying capacity of the masonry walls strengthened with CFRPs (Carbon Fiber Reinforced Polymer sheets), three pieces of masonry walls subjected to cyclic loads with low frequency and vertical load of constant amplitude have been tested. It is found that the critical loads the critical displacements, the ultimate loads, the ultimate displacements and the ductile coefficients of the masonry walls strengthened with CFRPs improve remarkably (6% similar to 57%). Therefore, the masonry structures strengthened with CFRPs are of better ductility and of better lateral load carrying capacity than the masonry structures without any strengthening measurements (Wei *et al.* 2007). In this paper, six specimens were tested under cyclic horizontal loads to study the deformation performance and the restoring model of the walls.

2. Test specimens and procedure

In this study, we have poured and constructed three groups of specimens of the multi-ribbed concrete columns and beams. Each group consists of two specimens. The first specimen was designed with C20 fine stone concrete and the other specimen was designed with M20 high strength mortar. The specimens were composed of insulation energy-saving blocks and an invisible multi-ribbed frame. The block was an aerated concrete block mainly composed of industry waste such as fly ash and furnace slag. The general view of blocks is shown in Fig. 1. There is a v-groove in each side of the block except the front and the rear ends, which was used to pour the invisible reinforced concrete columns (a prism with a 60-mm-long diagonal) and beams (the same size as the columns) that eventually formed the invisible multi-ribbed frame. A large outer frame was formed around the small concrete frame (shown in Fig. 2) by increasing the diameter of reinforcing steel bars at the both junctions of the wing sections, as well as the top or bottom beam of the main wall. The steel reinforcing arrangements of the specimens are shown in Table 1; the material mechanical properties (National Standard of the People's Republic of China 2002, 1998 and 2003) of the steel bar, the aerated concrete block and the concrete or mortar are shown in Tables 2~4 respectively.
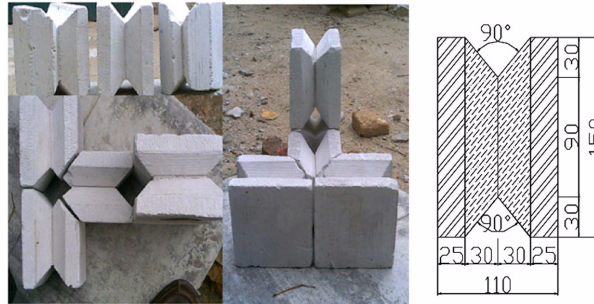
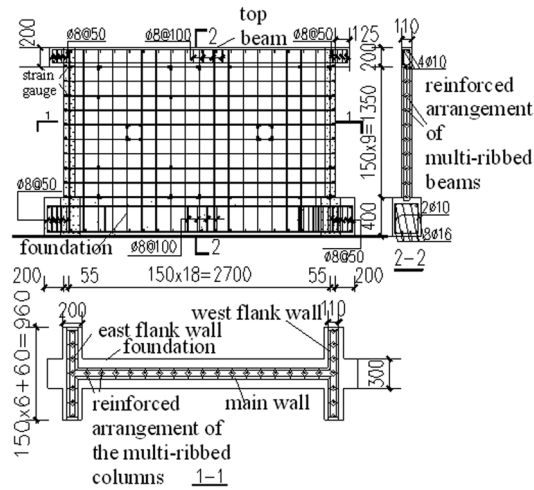Fig. 1 Abridged general view of the blocks and their combination form

Fig. 2 Multi-ribbed frame wall

Table 1 Design of specimens

Specimens	Reinforced arrangement (HPB235)			
	Outer rib column	Inner rib column	Top/bottom rib beam	Inner rib beam
EW1-1 EW1-2	1φ8 (2.79%)	1φ6 (1.57%)	1φ8 (2.79%)	1φ6 (1.57%)
EW2-1 EW2-2	1φ10 (4.36%)	1φ8 (2.79%)	1φ8 (2.79%)	1φ6 (1.57%)
EW3-1 EW3-2	2φ8 (5.61%)	2φ6 (3.17%)	1φ10 (4.36%)	1φ8 (2.79%)

Note: The figures in parenthesis are reinforcement ratio.

Table 2 Steel bar (HPB235) material mechanical properties test results

| Gauge	Diameter (mm)	Yield strength (MPa)	Ultimate strength (MPa)	Elastic modulus ($\times 10^5$N/mm^2)
φ6	6	248	331	2.1
φ8	8	276	310	2.1
φ10	10	289	306	2.1

Table 3 Aerated concrete block material mechanical properties test results

block material	Compressive strength (MPa)	Tensile strength (MPa)	Dry density (kN/m³)	Elastic modulus (N/mm²)
aerated concrete block	1.67	0.17	6	1105

Table 4 Concrete or mortar material mechanical properties test results

Specimens	Members	Designed strength grade of concrete or mortar	$f_{cu,m}$ (MPa)	f_{cm} (MPa)
EW1-1	multi-ribbed frame	C20	16.53	12.56
	top beam	C20	37.74	28.68
EW1-2	multi-ribbed frame	M20	16.45	12.50
	top beam	C20	22.80	17.33
EW2-1	multi-ribbed frame	C20	19.24	14.62
	top beam	C20	36.18	27.50
EW2-2	multi-ribbed frame	M20	17.51	13.31
	top beam	C20	22.74	17.28
EW3-1	multi-ribbed frame	C20	22.79	17.32
	top beam	C20	30.09	22.87
EW3-2	multi-ribbed frame	M20	17.16	13.04
	top beam	C20	21.97	16.70

Note: $f_{cu,m}$ is the mean value (the test value) of cubic compressive strength, f_{cm} is the mean value of prism compressive strength (because the test is carried out in the laboratory, modified factor is not considered, that is $f_{cm} = 0.76 f_{cu,m}$)
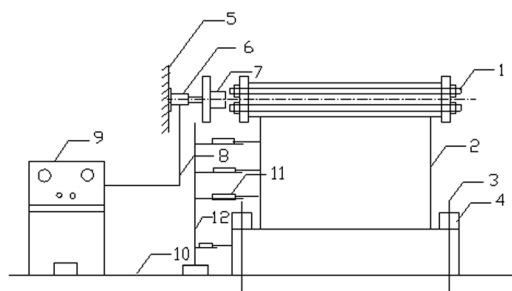
1.loading steel beam 2.specimen 3.anchor bolt 4.pressure beam

5.horizontal loading support frame 6.horizontal loading actuator

7.loading sensor 8.pipeline 9.Hydraulic Loading console

10.test platform 11.displacement meter 12.calibrating support
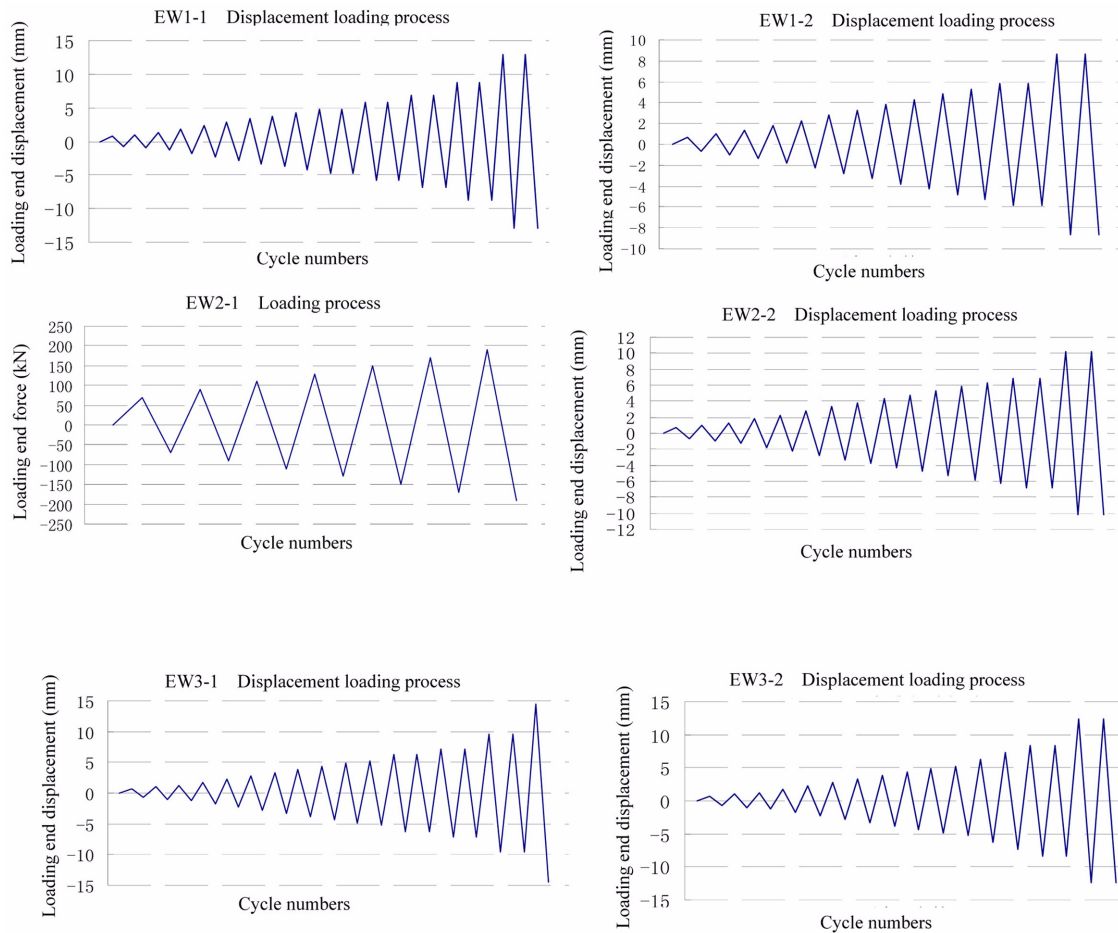
Fig. 3 Loading set-up

Fig. 4 displacement loading process of specimens

The loading set-up is shown in Fig. 3. Considering the worst-case scenario for the stress state, the low-cycle reversed lateral loading system was adopted on the basis of the comprehensive analysis of the test objectives and the loading apparatus. The horizontal load was applied on the ends of the beam by hydraulic actuator connected to the reaction frame. The procedure used displacement-control method. At first step we have used only one cycle for each incremental displacement before the specimen yielded. After the appearance of the yield point, we increased the number of cycles for each incremental displacement to two cycles until the specimen failed.

To simulate the mechanical behavior of a new building structure, an accurate finding on the actual mechanical performance was not possible for the model walls specimen. In the actual loading process of the test, based on establishing the initial loading criteria, the loading systems were adjusted according to the trend change of the hysteretic curve of every wall. The practical loading systems of every wall in this test are shown in Fig. 4.

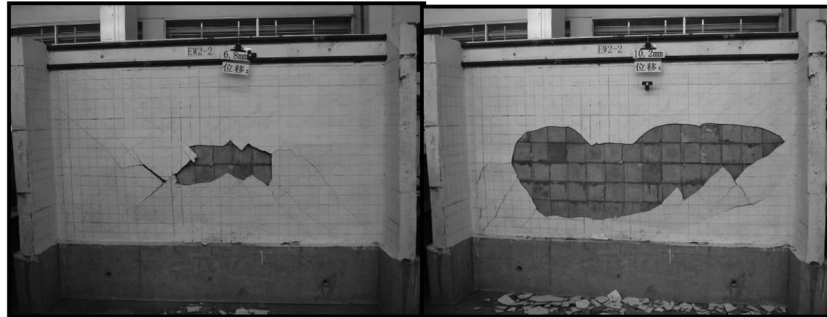Photos of the tested specimens are shown in Fig. 5.

Fig. 5 Photos of the tested specimens

3. Hysteretic characteristics and average skeleton curves

3.1 Hysteretic curves

3.4.1 Intercommunity of hysteretic curves of the model walls

From the hysteretic curves shown in Fig. 6, it's evident that the model masonry walls deformation is mainly elastic. Before initial cracking of the aerated concrete block, the shear force and displacement curves are basically linear. After the wall initially cracked while unloading the stiffness degenerative behavior of the model walls, the hysteretic loop's area under the curve is very small. As we increased the load, the cracks became larger, and the hysteretic curves pinched to a certain extent, but it was not very severe as we unloaded it to zero. Meanwhile, the hysteretic curves resemble a crescent moon shape, which means that no obvious shear deformation and slippage occurred. Then we continuously load the sample specimens to their ultimate load capacity to reach the stiffness degenerative behavior of the model walls. The hysteretic loops plumped and pinched significantly near the origin of the coordinates, and the hysteretic curves show a reversed S shape, because of the shear deformation and decline in hysteretic curves. In the loading cycle of the same displacement point, the loads basically became inferior by 25% and the hysteretic loops display the semi-steady condition. Henceforth, as the cyclic displacement increased step by step, the unloading flexural stiffness of the specimen became inferior rapidly, and the decline was extremely serious as a result of the spalling damage of the aerated concrete block, which is all reflected in the hysteretic curve as its middle section pinched seriously approaching the displacement axis as a result of the converse S shape.

3.1.2 The difference between the hysteretic curves

The initial flexural stiffness of the model wall EW1-2 was small in comparison to the others. Before the ultimate load (the load at ultimate displacement), the flexural stiffness of the two model walls EW3-1 and EW3-2 decreased quickly while the model wall EW1-1 exhibited much slower decline. As for the loading condition of the same displacement prior to the ultimate load, the loads of the specimens EW3-1 and EW3-2 deteriorated quickly while the load for the model wall EW1-1 deteriorated much slower. When the loading reached at 85% of the ultimate load, the hysteretic loops of the four model walls EW1-1, EW1-2, EW2-2 and EW3-2 showed relatively a full oblique shape (Fig. 6).
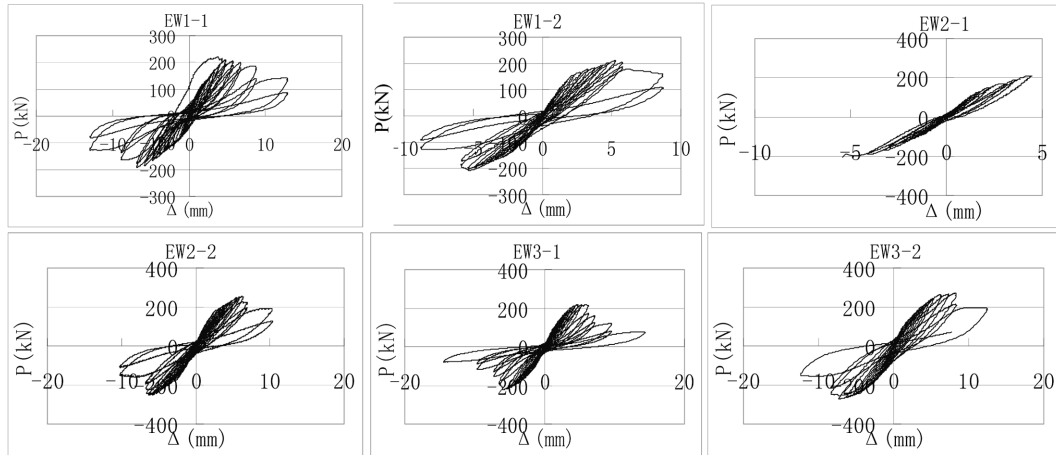
Fig. 6 Hysteretic curves of model walls

Table 5 The main seismic properties of multi-ribbed frame walls

Specimens	Cracking		Yield		Maximum		Ultimate		Ductil-ity factor
	P_{cr} (kN)	Δ_{cr} (mm)	P_y (kN)	Δ_y (mm)	P_m (kN)	Δ_m (mm)	P_u (kN)	Δ_u (mm)	
EW1-1	83.0	1.12	165.7	3.06	203.7	5.56	173.2	9.77	3.19
EW1-2	125.0	1.80	172.5	2.30	207.8	5.32	174.6	8.62	3.75
EW2-1	90.1	1.18	180.0	2.54	207.7	4.89	——	——	——
EW2-2	122.5	1.59	213.4	3.13	253.9	6.03	214.5	9.15	2.92
EW3-1	96.8	1.26	196.1	2.76	221.4	5.60	187.9	7.17	2.60
EW3-2	133.2	1.77	222.1	3.26	272.0	7.79	230.8	10.92	3.35

3.1.3 Conclusion

① As for the control specimens poured with the fine stone concrete in multi-ribbed beams and columns, the energy dissipation did not improve as the number of reinforcing steel bars increased. But for the poured multi-ribbed beams and columns with high strength mortar, the energy dissipation did improve as the number of reinforcing steel bars increased.

② Consequently, in the multi-ribbed beams and columns with the same displacement behavior and loading condition, the greater number of reinforcing steel bars, the quicker degenerative behavior of the load and flexural stiffness of the model walls.

3.2 Skeleton curves of shear force and displacement

The test characteristic values of the specimens under low-cycle reversed horizontal loads are shown in Table 5. The quadri-linear restoring model was applied to represent the skeleton curves of the models as the non-dimensional skeleton curves of the test under the same coordinates seemed to be in good adherence to each other. The initial cracking point A, the yield point B, the maximum
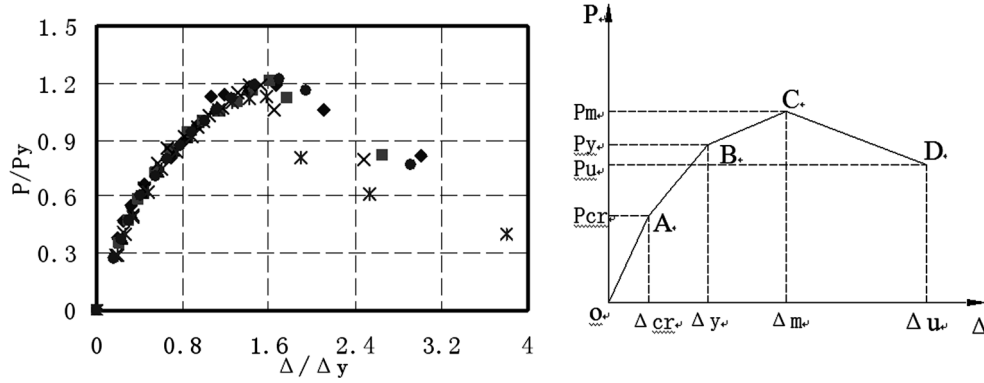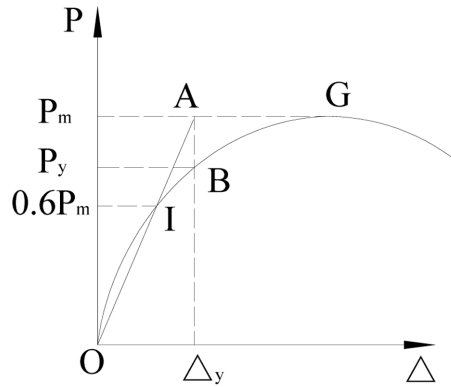
Fig. 7 Skeleton curves of model walls

Fig. 8 The Park graphic analysis method

load point C, and the ultimate load point D are the key points.

Likewise, the loads and displacements are: the cracking load P_{cr}, the cracking displacement Δ_{cr}; the yield load P_y, the yield displacement Δ_y; the maximum load P_m; the corresponding displacement Δ_m; the ultimate load P_u; the ultimate displacement Δ_u. (Fig. 7).

3.3 Definition of the main characteristic points

The initial crack was defined as the point where the first group of obvious cracks formed on the skeleton curve. The value of this point could be determined by the corresponding test data at the first crack point where the curve is turning. At the point of maximum load, the deformation increased rapidly while the load began to descend. Generally the ultimate load is defined as the maximum load descended to about 85% and the relative deformation was the ultimate deformation. In fact no clear yield point was obtained from the model walls. In order to discuss the deformation appropriately, the supposed yield point must be rationally determined. The Park graphic analysis method was used to analyze the skeleton curves of the model walls. With this method, the point I ($0.6\,P_m$) was determined on the skeleton curve in Fig. 8. Then we connected the origin point O and

point I to draw the line OI and extended it to get the intersecting point A and draw the horizontal line passed through point A to establish the ultimate load point G on the skeleton curve. The line AB was drawn vertically to the abscissa, which intersected point B on the skeleton curve, and designated as the equivalent yield point. From Fig. 8 we can observe that the supposed yield load was determined as $0.85 P_m$, and the relative lateral displacement as Δ_y.

3.4 Evaluation of the ductility capacity of RGMACBMW

Taking the lateral displacement Δ_y of the model walls at assumed yield point as its yield displacement, the average lateral displacement ductility factor of RGMACBMW calculated by test results was 3.16. This value illustrates that the model walls were properly designed and they meet seismic requirements of the structures. In China and abroad the range of values in displacement ductility factor of the structure is generally between 3 to 5, one can observe from Table 5 that the model walls EW1-1, EW1-2 and EW3-2 have ductility factors larger than 3, which are satisfactory. However, the model walls ductility seems to descend instead of escalation even with the increase of the steel reinforcement bar members. Therefore, the failure mode of the model walls was mainly a shear force failure, and the rationally designed model walls could still be within the allowable deformability. The "rationally design" here referred to a rational shearing-compression ratio and arrangement of the reinforcement of multi-ribbed beams and columns. So as to form rational failure mechanism of wall, the wall fails in the following order: firstly, the cracking of blocks, secondly the cracking of the small inner multi-ribbed frame, thirdly cracking of the large outer frame, fourthly reinforcement yielding of the small inner multi-ribbed beam, fifthly reinforcement yielding of the small inner multi-ribbed column, after that reinforcement yielding of the large outer frame beam, and then reinforcement yielding of the large outer frame column and concrete crushing.

4. Shear capacity formula

The blocks in the multi-ribbed frame members play a role of diagonal strut under the horizontal shear force. Moreover, the interaction between the horizontal shear force of the blocks and the multi-ribbed frame structure exhibits the bending moment of the columns and beams to be very small, hence the columns and beams in the multi-ribbed frame structure are considered to be the main member bearing axial force.

The shear capacity of RGMACBMW in the nominal failure diagonal section is equated as the following

$$V = V_c + V_{ck} + V_q + V_{qk} + V_{sh} + V_{sv} \tag{1}$$

Where V is the shear capacity of the walls; V_c is the shear capacity of the grout material on un-cracked areas in nominal failure diagonal section; V_{ck} is the shear capacity of the grout material on cracked areas in nominal failure diagonal section; V_q is the shear capacity of aerated concrete blocks on un-cracked areas in nominal failure diagonal section; V_{qk} is the shear capacity of aerated concrete blocks on cracked areas in nominal failure diagonal section; V_{sh} is the shear capacity of multi-ribbed beam reinforcement bars; V_{sv} is shear capacity of multi-ribbed column reinforcement bars (dowel resistance of the longitudinal bars etc.).

To evaluate the shear capacity of the walls, the following formula is obtained

$$V = \frac{1}{\lambda - 0.5}[0.09(f_{ca}A_{ca}+f_{q}A_{q})+0.12f_{cz}A_{cz}+0.06f_{cl}A_{cl}]+[0.42f_{ya}A_{sa}+0.28f_{yz}A_{sz}+1.05f_{yl}A_{sl}] \tag{2}$$

Where λ is the height-width ratio of the walls ($\lambda = H/L$) and is called the shear span ratio of the section, it ranges between 1.5 and 2.2; A_{ca}, A_{q}, A_{cz}, and A_{cl} are the sectional areas of the large outer frame column, the aerated concrete blocks (not including those sections of the flanges only the horizontal cross-section of the blocks), the small inner multi-ribbed column (not including those sections of the flanges) and the small inner multi-ribbed beam (not including those sections of the flanges) respectively; f_{ca}, f_{q}, f_{cz}, and f_{cl} are the design compressive strength values of grout material of the large outer frame column, the aerated concrete blocks, the grout material of small inner multi-ribbed column and the small inner multi-ribbed beam respectively; f_{ya}, f_{yz} and f_{yl} are the design tensile strength values of steel reinforcement bars in the large outer frame column, the small inner multi-ribbed column and the small inner multi-ribbed beam respectively; A_{sa}, A_{sz}, and A_{sl} are the sectional areas of steel reinforcement bars in the large outer frame column, the small inner multi-ribbed column and the small inner multi-ribbed beam respectively.

5. Stiffness calculations of all stress stages and restoring force model

5.1 Average stiffness K_1 before cracking

Through the observation of the skeleton curves of RGMACBMW in Fig. 7, the model walls were basically in elastic condition before any cracking. Therefore, the model wall with the adjoining wall could be simplified as I-shape section beam and the average flexural stiffness can be obtained by elastic theory.

As shown in Fig. 9, the displacement δ was called lateral flexibility when a unit force was applied to the top end of the model wall, the lateral stiffness is the reciprocal of the lateral flexibility: $K = 1/\delta$.

Assuming that the model wall is a cantilever structural member, and the total deformation of the model wall was composed of the flexural deformation δ_b and the shearing deformation δ_s under the horizontal unit force. So the elastic lateral stiffness of the homogeneous model wall is calculated as Eq. (3)

$$K = \frac{1}{\delta_b + \delta_s} = \frac{1}{\left(\dfrac{H^3}{3EI}+\dfrac{\mu H}{GA}\right)} \tag{3}$$

Where H represents the height of wall; A is the area of the wall cross section (I-shape section); μ is the shearing stress coefficient of the model wall for I-shape section $\mu = A/A'$, where A' is the area of the web section; I represents the moment of inertia for the I-shape section; E is the elastic modulus; and G represents the shearing modulus.

The reinforced grouted multi-ribbed aerated concrete blocks masonry structure was composed of energy-saving blocks and an invisible multi-ribbed frame. The elastic moduli of two parts were
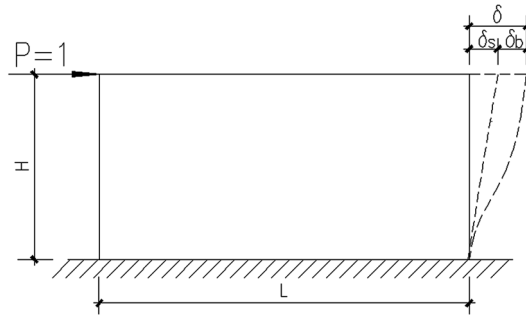
Fig. 9 Flexural deformation and shearing deformation of model wall under a unit force

Table 6 Calculated results of the lateral stiffness

Specimens	K_1 (kN/mm)	K_0 (kN/mm)	K_1/K_0
EW1-1	74.11	88.70	0.84
EW1-2	69.44	88.67	0.78
EW2-1	76.36	89.36	0.85
EW2-2	77.04	88.94	0.87
EW3-1	76.83	90.04	0.85
EW3-2	75.25	88.87	0.85

Note: K_1 is the experimental initial stiffness, and K_0 is the analytical initial stiffness

different to a large extent, so the elastic lateral flexural stiffness of the homogeneous model wall could not be calculated directly (Zhao *et al*. 1999). The composite material method (Wang 2003) was applied to calculate and figure out the elastic constants of the model wall. Hence the elastic lateral flexural stiffness could be calculated by the preceding formula in Eq. (3). The calculated results are shown in Table 6.

Through the test of the whole bearing wall member composed of energy-saving blocks and an invisible multi-ribbed frame, the deformation capacity and the common behavior of all its components have been maintained until the blocks failed. In macroscopic view, the wall was an elastic composite panel with energy-saving blocks being the main body and concrete rib beams, columns and outer frame as reinforcing fiber. A simplified model of the wall panel is shown in Fig. 10. Based on the equivalent principle the concrete volume ratio of the wall remained unchanged, this was contributed by the concrete rib beams, columns and outer frame having a large quantity of fine aggregates homogeneously and uniformly distributed through out the matrix which is composed of energy-saving blocks. Therefore, the wall was considered as an orthotropic fiber-reinforced elastic composite panel.

Theoretically based on the stiffness calculation for an orthotropic fiber-reinforced composite material we can calculate the stiffness characteristics of the wall. Since the mechanical property of the orthotropic materials is very complicated; a more simplified method of calculation was ascertained for isotropic materials. This simplified method considers the average elastic modulus
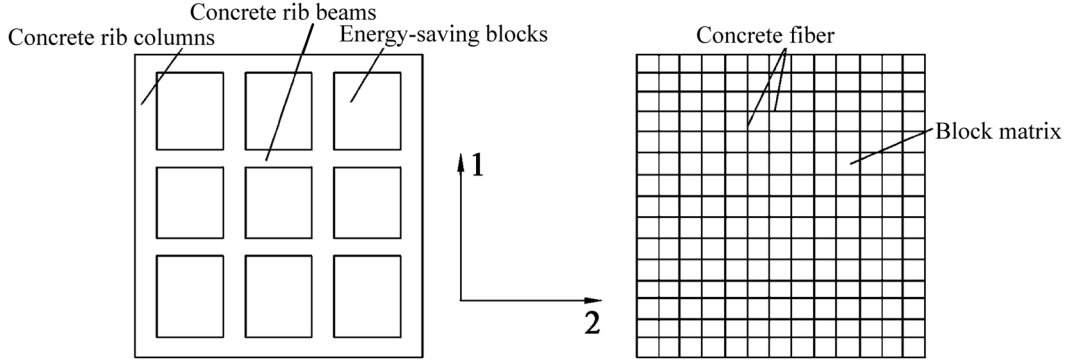
Fig. 10 A simplified material model of the wall

value of the two directional orthotropic fiber-reinforced elastic composite panel models; and the shear modulus of the orthotropic fiber-reinforced elastic composite panel model.

The flexural stiffness before cracking of every specimen was calculated by Eq. (3). The calculated results were 15% higher than the experimental results in average. This was contributed due to the continuous development of the hairline cracks of RGMACBMW prior to the formation of any visible cracks. Therefore, Eq. (3) must be modified as: $K_1 = 0.85K$.

5.2 The stiffness of the model walls after cracking

The model walls exhibit a nonlinear performance after the initial crack. There has been a change in the force transferring mechanism. At this point, the model walls restrained by the exterior frame formed a resisting lateral force system which consisted by the oblique-compression bar and the tension reinforcement. Since the stress calculation for this experiment is very complicated, and solving the deformation of the model walls theoretically becomes very difficult. Therefore, the statistical method was applied to solve the stiffness of the model walls.

Through observation from the skeleton curves in Fig. 7, the following four main characteristic points (the initial crack point, the yield point, the maximum point and the ultimate point), the lateral displacement and loading coordinates were obtained respectively: (1.45, 108.43), (2.84, 191.63), (5.87, 227.75) and (9.13, 196.20). Presumably the stiffness after cracking is $K_2 = \alpha_2 K_1$, the stiffness after yielding is $K_3 = \alpha_3 K_1$ and the stiffness after the maximum loading is $K_4 = \alpha_4 K_1$, the following results were calculated from the geometric relation in Fig. 5 that $\alpha_2 = 0.80$, $\alpha_3 = 0.16$, $\alpha_4 = -0.13$.

5.3 Determination of load and displacement of every feature points

The shear capacity, maximum load P_m was calculated according to formula (2).

The initial cracking load of the specimens which were manufactured using C20 concrete was calculated using the following formula (4)

$$P_{cr} = 0.43P_m \tag{4}$$

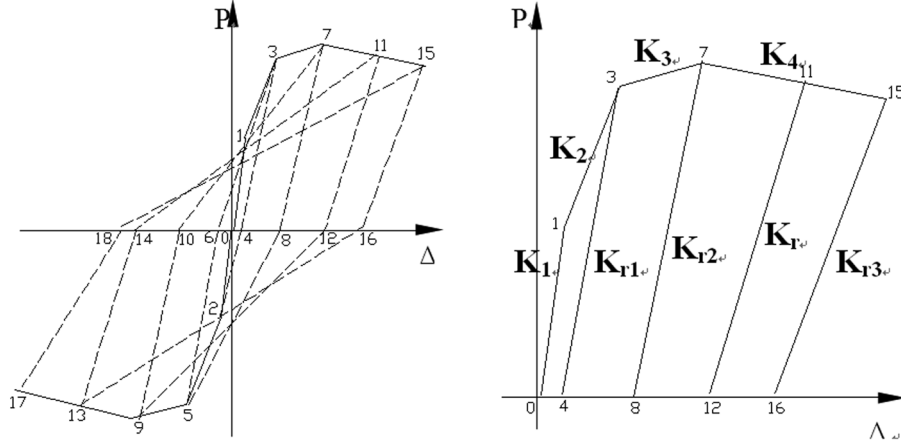The initial cracking load of the specimens which were manufactured using M20 mortar was

Fig. 11 The restoring model of model

calculated using the following formula (5)

$$P_{cr} = 0.52P_m \tag{5}$$

The yield load and ultimate load was calculated according to formula (6)

$$P_y = P_u = 0.85P_m \tag{6}$$

The cracking displacement was calculated according to formula (7)

$$\Delta_{cr} = P_{cr}/K_1 \tag{7}$$

The yield displacement was calculated according to formula (8)

$$\Delta_y = (P_y - P_{cr})/K_2 + \Delta_{cr} \tag{8}$$

The displacement of maximum load was calculated according to formula (9)

$$\Delta_m = (P_m - P_y)/K_3 + \Delta_y \tag{9}$$

The ultimate displacement was calculated according to formula (10)

$$\Delta_u = (P_u - P_m)/K_4 + \Delta_m \tag{10}$$

5.4 The restoring model of specimens

For the specimens a gradual failure process was designed and the test procedure was used to

demonstrate the design principle of energy–dissipation. Combining the skeleton curves and the flexural stiffness degeneration of the model walls, considering the practical rules to define the maximum point on the curve when the load is applied in the opposite direction, the degrading quadrilinear restoring force model (see in Fig. 11) was chosen in the paper as shown below (Tomazevic *et al*. 1996, Tomazevic and Lutman 1996). In Tomazevic and Lutman's restoring force model, the skeleton curve is a simple symmetric, tri-linear hysteresis envelope, determined by three pairs of values of lateral load and displacement, which define the cracking point, maximum resistance, and ultimate limit state of the behavior of a wall respectively. The shortcoming of the Tomazevic and Lutman's restoring force model was that there is no yield point; hence we have chosen to overcome this shortcoming and determine the degrading quadrilinear restoring force model in this paper. By comparing the results in this paper with the models developed by Tomazevic and Lutman, the hysteretic behavior of the two experiments are quite similar except the yield point.

5.4.1 The loading stiffness

The transformation rule on the loading stiffness is shown in Fig. 11; the elastic stage (0-1) and the elastic stiffness K_1; the elastic-plastic stage (1-7), the stiffness K_2 before yield (1-3) and K_3 after yield (3-7); the failure stage (7-15) and the negative stiffness K_4. According to the test results and statistical data, the stiffness of every stage could adopt the recommendation in section 5.2. The initial crack point, yield point, maximum point, ultimate point were determined respectively according to the preceding definition and statistical data.

5.4.2 The unloading stiffness

This paper has chosen the degrading quadrilinear model for the restoring model walls. The degrading rule of stiffness is mainly related to the unloading stiffness shown in Fig. 7. Based on the normal hysteretic loops obtained from the statistical data at the yield point, the maximum point, the ultimate point, and the model walls unloading stiffness constructed at three stages were interpolated. To calculate the described conditions the following formulas were considered (For an explanation of the symbols referring to 3.2)

$$K_{r1} = (\Delta_{cr}/\Delta_r)^{0.5} K_1 \qquad (\Delta_{cr} < \Delta_r < \Delta_y) \tag{11}$$

Table 7 The calculation results of stiffness

Specimens	K	K_1	K_2	K_3
EW1-1	88.70	75.40	60.32	12.06
EW1-2	88.67	75.37	60.30	12.06
EW2-1	89.36	75.96	60.77	12.15
EW2-2	88.94	75.60	60.48	12.10
EW3-1	90.04	76.53	61.22	12.24
EW3-2	88.87	75.54	60.43	12.09

Table 8 Comparison of the test and calculation results for the significant points of the skeleton curve

Specimens	P_{cr} (kN)		Δ_{cr} (mm)		P_y (kN)		Δ_y (mm)	
	$P_{cr.e}$	$P_{cr.c}$	$\Delta_{cr.e}$	$\Delta_{cr.c}$	$P_{y.e}$	$P_{y.c}$	$\Delta_{y.e}$	$\Delta_{y.c}$
EW1-1	83.0	86.47	1.12	1.15	165.7	170.94	3.06	2.55
EW1-2	125.0	104.26	1.80	1.38	172.5	170.43	2.30	2.48
EW2-1	90.1	93.91	1.18	1.24	180.0	185.64	2.54	2.75
EW2-2	122.5	128.02	1.59	1.69	213.4	209.27	3.13	3.03
EW3-1	96.8	108.53	1.26	1.42	196.1	214.54	2.76	3.15
EW3-2	133.2	140.35	1.77	1.86	222.1	229.42	3.26	3.33

Specimens	P_m (kN)		Δ_m (mm)		P_u (kN)		Δ_u (mm)	
	$P_{m.e}$	$P_{m.c}$	$\Delta_{m.e}$	$\Delta_{m.c}$	$P_{u.e}$	$P_{u.c}$	$\Delta_{u.e}$	$\Delta_{u.c}$
EW1-1	203.7	201.1	5.56	5.05	173.2	170.94	9.77	8.13
EW1-2	207.8	200.5	5.32	4.97	174.6	170.43	8.62	8.04
EW2-1	207.7	218.4	4.89	5.45	—	185.64	—	8.77
EW2-2	253.9	246.2	6.03	6.08	214.5	209.27	9.15	9.84
EW3-1	221.4	252.4	5.60	6.24	187.9	214.54	7.17	10.05
EW3-2	272.0	269.9	7.79	6.68	230.8	229.42	10.92	10.80

$$K_{r2} = (\Delta_y/\Delta_r)^{0.61} K_1 \qquad (\Delta_y < \Delta_r < \Delta_m) \tag{12}$$

$$K_{r3} = (\Delta_m/\Delta_r)^{0.63} K_1 \qquad (\Delta_m < \Delta_r < \Delta_u) \tag{13}$$

Where K_{ri} ($i = 1, 2, 3$) represents the unloading stiffness and Δ_r represents the lateral displacement of the model walls when unloaded.

5.5 Fitting of feature points of skeleton curve

Based on the method in section 5.2 and 5.3, the flexural stiffness and feature points of the skeleton curve of RGMACBMW have been calculated. The results of the flexural stiffness are shown in Table 7.

The test results and calculations of the feature points are shown in Table 8. In table 8 the subscript e represents the experimental values and subscript c represents the calculation results respectively.

The Comparison of the calculated and test results are shown in Fig. 12. Through observation the test results are fairly close to the calculated values for the skeleton curves in this paper.
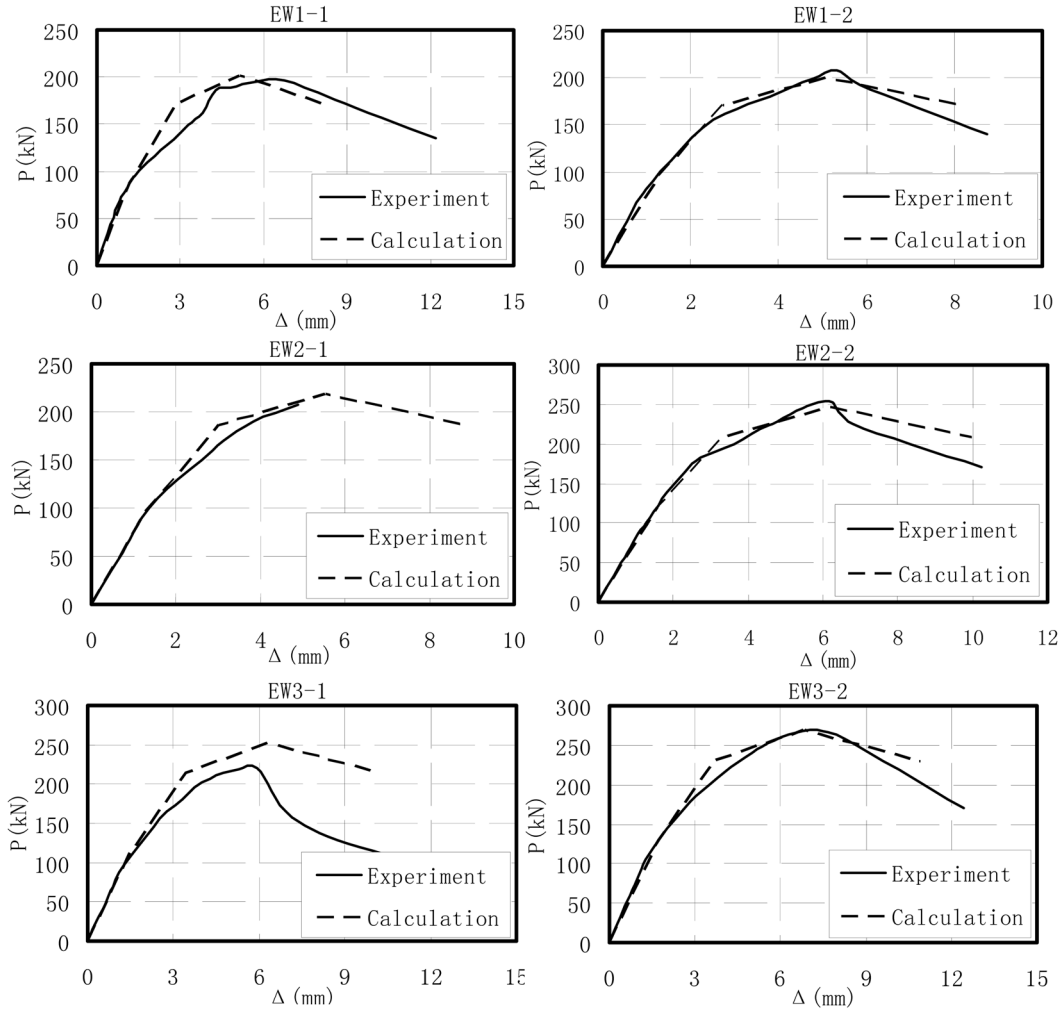
Fig. 12 Comparison on skeleton curves of calculation and test results

6. Conclusions

(1) The ductility factor of the average lateral displacement for RGMACBMW is 3.16 which was calculated and supported by the test results. This value illustrates that the model walls rationally designed can meet the seismic requirements of the structure. Therefore, the general failure mode of the model walls was due to the shear failure under the low-cycle reversed lateral loads. However, the model walls that are rationally designed would possess certain deformation capacity.
(2) Through the accurate experimental data of RGMACBMW, the degradation quadrilinear restoring model was obtained for the model walls, which by comparison correctly reflect the hysteretic property and skeleton curves of the model walls. Therefore, the restoring model can be applied to the time-history analysis of the reinforced grouted multi-ribbed aerated concrete blocks masonry structure.

(3) Based on the Pseudo Static Test the restoring model proposed in this paper could not comprehensively reflect the real dynamic performance of RGMACBMW. It is recommended that a more comprehensive study of the seismic performance of the pseudo dynamic test or the shaking table test to be carried out.

Acknowledgments

References

Atkinson, R.H. and Hammons, M.I. (1997), "Tension Stiffening Behavior of Reinforced Masonry", *J. Struct. Eng.*, **123**(5), 597-603.

Drysdale, R.G. and Khattab, M.M. (1995), "In-Plane Behavior of Grouted Concrete Masonry under Biaxial Tension-Compression", *ACI Struct. J.*, **92**(6), 653-664.

Li, S.C. and Zeng, Z.X. (2005), "Research on energy-saving block and invisible multi-ribbed frame structure", *Proceeding of the third specialty conference on the conceptual approach to structural design*, Singapore, August.

National Standard of the People's Republic of China, (1998) "Test Methods of Aerated concrete", (GB/T11969~11975-1997[S], Standards Press of China, Beijing. (in Chinese)

National Standard of the People's Republic of China (2002) "Metallic Materials Tensile Testing at Ambient Temperature", (GB/T 228-2002) [S], Standards Press of China, Beijing. (in Chinese)

National Standard of the People's Republic of China (2003) "Standard for test method of mechanical properties on ordinary concrete", (GB/T50081-2002) [S], China Architecture and Building Press, Beijing. (in Chinese)

Shedid, M., Drysdale, R.G. and El-Dakhakhni, W. (2008), "Behavior of Fully Grouted Reinforced Concrete Masonry Shear Walls Failing in Flexure: Experimental Results", *J. Struct. Eng.*, **134**(11), 1754-1767.

Shedid, M., Drysdale, R.G. and El-Dakhakhni, W. (2009), "Behavior of fully grouted reinforced concrete masonry shear walls failing in flexure: analysis", *Eng. Struct.*, **31**(9), 2032-2044.

Shing, P.B., Schuller, M. and Hoskere, V.S. (1990a), "In-plane resistance of reinforced masonry shear walls", *J. Struct. Eng.*, ASCE, **116**(3), 619-640.

Shing, P.B., Schuller, M., Hoskere, V.S., and Cater, E. (1990b), "Flexural and shear response of reinforced masonry walls", *ACI Struct. J.*, **87**(6), 646-656.

Tikalsky, P.J., Atkinson, R.H. and Hammons, M.I. (1995), "Compressive Strength of Reinforced Masonry under Lateral Tension", *J. Struct. Eng.*, **121**(2), 283-289.

Tomazevic, M., Lutman, M. and Petkovic, L. (1996), "Seismic behaviour of masonry walls: experimental simulation", *J. Struct. Eng.*, ASCE, **122**(9), 1040-1047.

Tomazevic, M. and Lutman, M. (1996), "Seismic behaviour of masonry walls: modelling of hysteretic rules", *J. Struct. Eng.*, ASCE, **122**(9), 1048-1054.

Voon, K.C. and Ingham, J.M. (2006), "Experimental in-plane shear strength investigation of reinforced concrete masonry walls", *J. Struct. Eng.*, ASCE, **132**(3), 400-408.

Voon, K.C. and Ingham, J.M. (2007), "Design expression for the in-plane shear strength of reinforced concrete masonry", *J. Struct. Eng.*, ASCE, **133**(5), 706-713.

Wang, Z.M. (2003), *Composite Materials Mechanics and Composite Materials Structural Mechanics*, Science Press, Beijing. (in Chinese)

Wei, C.Q., Zhou, X.G. and Ye, L.P. (2007), "Experimental study of masonry walls strengthened with CFRP", *Struct. Eng. Mech.*, **25**(6), 675-690.

Zhai, X. and Stewart, M.G. (2010), "Structural reliability analysis of reinforced grouted concrete block masonry walls in compression", *Eng. Struct.*, **32**(1), 106-114.

Zhao, D., Yao, Q.F. and Chen, P. (1999), "Lateral rigidity calculation of multi-ribbed lightweight frame", *J. Xi'an Univ. Architect. Technol.*, **31**(3), 18-21. (in Chinese)